Promoting Atomically Dispersed MnN_4 Sites *via* Sulfur Doping for Oxygen Reduction: Unveiling Intrinsic Activity and Degradation in Fuel Cells

Lin Guo,[†,≠] Sooyeon Hwang,[‡,≠] Boyang Li,[⊥,≠] Fan Yang,[&] Maoyu Wang,[◊] Mengjie Chen,[†]
Xiaoxuan Yang,[†] Stavros G. Karakalos,[Δ] David A. Cullen,[#] Zhenxing Feng,[◊]* Guofeng
Wang,[⊥]* Gang Wu[†]* and Hui Xu [&]*

† Department of Chemical and Biological Engineering, University at Buffalo, The State University of New York, Buffalo, NY 14260, USA.

‡ Center for Functional Nanomaterials Brookhaven National Laboratory Upton, NY 11973, USA.

⊥ Department of Mechanical Engineering and Materials Science, University of Pittsburgh, Pittsburgh, PA 15260, USA.

& Giner Inc, Newton, MA 02466, USA.

◊ School of Chemical Biological, and Environmental Engineering, Oregon State University, Corvallis, OR 97331, USA.

Δ Department of Chemical Engineering, University of South Carolina, Columbia, SC 29208, USA.

Materials Science and Technology Division, Oak Ridge National Laboratory, Oak Ridge, TN 37831, USA.

ABSTRACT: Carbon supported and nitrogen coordinated single Mn site catalysts (Mn-N-C) catalysts are the most desirable platinum group metal (PGM)-free cathode catalysts for proton exchange membrane fuel cells (PEMFCs) due to their insignificant Fenton reactions (*vs*. Fe), earth abundances (*vs*. Co), and encouraging activity and stability. However, current Mn-N-C catalysts suffer from high over-potential due to low intrinsic activity and less dense MnN_4 sites. Herein, we present sulfur-doped Mn-N-C catalyst (Mn-N-C-S) synthesized through an effective adsorption-pyrolysis process. Using electron microscopy and X-ray absorption spectroscopy (XAS) techniques, we verify the uniform dispersion of MnN_4 sites and confirm the effect of S doping on the Mn-N coordination. The Mn-N-C-S catalyst exhibits a favorable oxygen reduction reaction (ORR) activity in acidic media relative to the S-free Mn-N-C catalyst. The corresponding membrane electrode assembly (MEA) generated enhanced performance with a peak power density of 500 mW cm^{-2} under a realistic H_2/air environment. The constant voltage tests of fuel cells confirm the much-enhanced stability of the Mn-N-C-S catalyst compared to the Fe-N-C and Fe-N-C-S catalysts. The electron microscopy and Fourier transform XAS analysis provide insights into catalyst degradation associated with Mn oxidation and agglomeration. The theoretical calculation elucidates that the promoted ORR activity is mainly attributed to the spatial effect stemmed from the repulsive interaction between the ORR intermediates and adjacent S dopants.

KEYWORDS: sulfur doping; single metal site; oxygen reduction; electrocatalysis; fuel cells

The atomically dispersed transition metal and nitrogen co-doped carbon materials (M-N-C, M: Fe, Co, Mn, *etc*.) have emerged as the most promising catalysts for oxygen reduction reaction (ORR) in proton exchange membrane fuel cells (PEMFCs) because of their low cost, high utilization of metal, and promising catalytic activity.[1-5] Among all these catalysts to date, Fe-N-C catalysts have exhibited promising activity in acidic media.[6] However, the Fe-N-C catalysts have not yet met the requirement for the practical operation of PEMFCs owing to the rapid loss of FeN_4 active sites under practical operating conditions.[7-10] More importantly, the dissolved Fe ions can intensively accelerate the Fenton reactions, thus producing large amounts of oxygen-containing radical species, which not only lead to the dramatic degradation of membrane and ionomer in the catalytic layer, but also severely damage the triple-phase interface and the proton passways in PEMFCs.[11-13] Therefore, the reactions triggered by dissolved Fe ions drastically accelerate the decay of the overall PEMFC performance.

Compared to Fe ions, Mn ions barely react with hydrogen peroxide and show a Fenton-inactive character.[14] Density functional theory (DFT) studies predicted that the MnN_4 structure is an active center and follows a 4-electron transfer pathway during the ORR.[15-17] The experiment results have further revealed that Mn-based catalysts have moderate ORR activity in acidic and alkaline media.[18-20] Besides, compared to extensively studied CoN_4 sites,[3, 21-24] MnN_4 sites have enhanced intrinsic activity for the ORR due to the more optimal adsorption of O_2 and reduced activation energy to break O-O bond.[16, 25] Accordingly, Mn-N-C catalysts appear to be a promising alternative to replace Fe-N-C catalysts to address the possible Fenton reaction issue. However, due to the low density of active sites, the current activity of Mn-N-C catalysts is far below the commercialization requirements of PEMFCs. Thus, extensive materials and strategies have been proposed to improve the activity of Mn-N-C catalysts, mainly focusing on excessive usage of Mn source in synthesis processes.[2, 16, 26] A doping-adsorption method was developed by our group to prepare atomically dispersed M-N-C catalysts, in which the metal sites can be introduced into carbon matrix step by step to increase the MN_4 site density. These prepared catalysts exhibited improved catalytic activity and promising stability.[2, 23, 27-28] Besides the site density, the optimal catalyst morphologies are critical to maximizing the accessible active sites in 3D porous catalysts.[29-31] Recently, we developed an environmentally friendly approach to synthesizing Mn-N-C catalysts to inhibit the agglomeration.[32] The synthesis strategy yielded a curved surface structure for the Mn-N-C catalyst with high surface areas, which benefits from introducing accessible MnN_4 moieties and improving mass transport.

Despite the above successes, the catalyst activity is mainly achieved by increasing the density of MnN_4 sites and optimizing catalyst morphologies. To break the activity limit and achieve precise control of local coordination of active sites, one strategy is to introduce additional heteroatoms to enhance the intrinsic activity of MnN_4 sites, while maintaining a reasonable active site density at the surface of the catalyst. The interaction can change the adsorption strength of the intermediates during the ORR, thus improving the intrinsic activity of the catalyst.[33-35] Recent works have revealed that introducing sulfur element with a relatively larger atomic radius and lower electronegativity compared to N element can generate additional defects and interaction with active sites.[36-38] Moreover, the C-S-C structure increases the hydrophobicity of carbon materials,[39] which is highly desirable for improving water management in thick cathodes. Inspired by the previous researches, we hypothesized that the S-doped Mn-N-C catalysts could enhance the ORR activity and fuel cell performance. To our best knowledge, there has been no extensive investigation to elucidate the effect of the S doping on the catalytic activity of the MnN_4 active center.

Herein, we report an Mn-N-C-S catalyst prepared by an adsorption process followed by effective thermal activation. Unlike the previously reported works,[2, 32] the current synthesis method improves the ORR activity through successfully introducing S element to the porous carbon framework, instead of the formation of inactive particles, and time-consuming acid-leaching treatment. The Mn-N-C-S catalyst exhibited significantly enhanced catalytic ORR activity than traditional Mn-N-C catalysts (**Table S1**), and demonstrated a peak power density of ~0.500 W cm^{-2} in a membrane electrode assembly (MEA) under H_2-air conditions. The introduction of S element increases the surface area of the Mn-N-C-S catalyst, restructures the carbon matrix, compresses the space of Mn-N bonding, and provides the repulsive effect on ORR intermediate species absorbed on the MnN_4 site. Furthermore, the in-depth investigation of changes in the active site structure upon the stability test sheds light on the Mn-N-C-S catalyst's degradation mechanisms in MEAs.

RESULTS AND DISCUSSION

Catalyst Synthesis, Morphology, and Structures. The Mn-N-C-S catalyst was prepared through an adsorption-pyrolysis process, as illustrated in **Figure 1a**. In brief, ZIF-8 nanocrystals were synthesized *via* the modified solvothermal method we previously developed.[40] Subsequently, the obtained ZIF-8 particles were carbonized at 900 °C for one hour and converted into nitrogen-doped carbon. Afterward, the nitrogen-doped carbon with porous structure was immersed in a mixed solution of $MnCl_2$ and thiourea, and collected after centrifugation and vacuum-dry followed by pyrolysis at 1100 °C for one hour. During the high-temperature treatment, the Mn and S were doped into the carbon, and the residual Zn in the carbon host was evaporated simultaneously. The resultant product was denoted as the Mn-N-C-S catalyst.

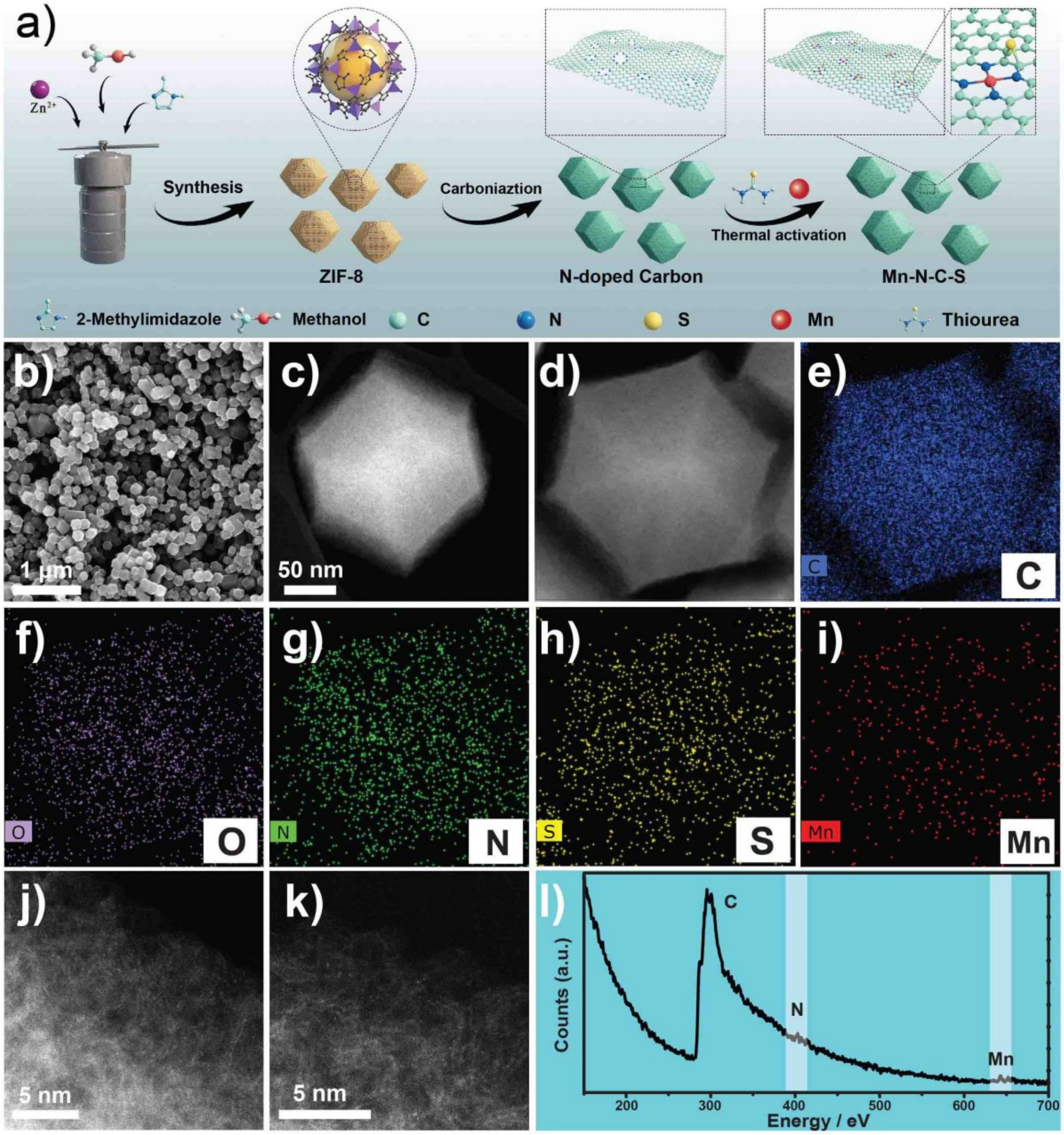

Figure 1. (a) Schematic diagram of the formation processes of the Mn-N-C-S catalyst. Morphology, composition, and atomic structure of Mn-N-C-S catalyst. (b) SEM image, (c, d) STEM images, and (e-i) EDS mapping images of an individual Mn-N-C-S catalyst nanocrystal; (j, k) HAADF-STEM images, and (l) EEL spectrum, the point spectrum from the atomic sites pointed at yellow dot in Figure S2b.

Typical scanning electron microscopy (SEM) images (**Figure 1b** and **Figure S1**) show that the Mn-N-C-S catalyst consists of highly monodispersed polyhedral nanoparticles with a diameter of ca. 160 nm. The dark-field scanning transmission electron microscopy (STEM) images (**Figure 1c, d,** and **Figure S2a**) display that the single polyhedral particle has a uniform inner structure without encapsulated metal nanoparticles inside, implying that no Mn-based particles exist in the catalyst. The EDS elemental mapping was obtained to analyze the elemental distribution of catalysts. As shown in **Figure 1e-i** and **Figure S3**, six elements (C, O, N, S, Mn, and Zn) are uniformly distributed throughout the entire particles, consistent with the characterization results of SEM-EDS in **Figure S4**. Based on the high vacuum and high energy rays in the TEM chamber, the signal that contributes to the EDS detector should originate from the stable chemical species. Both S and Mn signals in EDS elements mapping provide strong evidence for the successful doping of S and Mn elements in the Mn-N-C-S catalyst. XRD analysis was performed to determine the crystalline structure of the obtained catalyst. As shown in **Figure S5**, two broad peaks at 24° and 43° can be indexed to the diffraction from (002) and (101) planes of typical amorphous carbon, respectively.[41-42] The XRD patterns confirmed that the catalysts are composed of porous carbon material with low graphitization, which agrees with the STEM results. No peaks of Mn, MnO, and/or MnS were detected in the XRD pattern, further confirming the possible absence of crystalline Mn-base particles in the catalyst. **Figure 1j** and **k** obtained by the high-angle annular dark-field scanning TEM (HAADF-STEM) show that bright dots associated with massive atomically dispersed Mn sites are homogeneously embedded into disordered porous carbon with randomly oriental graphitic domains, confirming that Mn elements are atomically dispersed on S, N co-doped carbon. Meanwhile, the single Mn sites' chemical environment was determined by the HAADF-STEM coupled with electron energy loss spectroscopy (EELS). As depicted in **Figure 1l**, Mn and N's signals are observed in the EELS spectrum at the atomic level. Considering the EELS electron beam angstrom solution and high energy, the signals are definitely attributed to the stable chemical structure of the center atom and its adjacent atoms, indicating the existence of the Mn-N coordination in the Mn-N-C-S catalyst. There are no apparent signals of S and O elements in the EELS spectrum, further verifying that Mn has no chemical bonding with S and/or O in Mn-N-C-S catalysts.

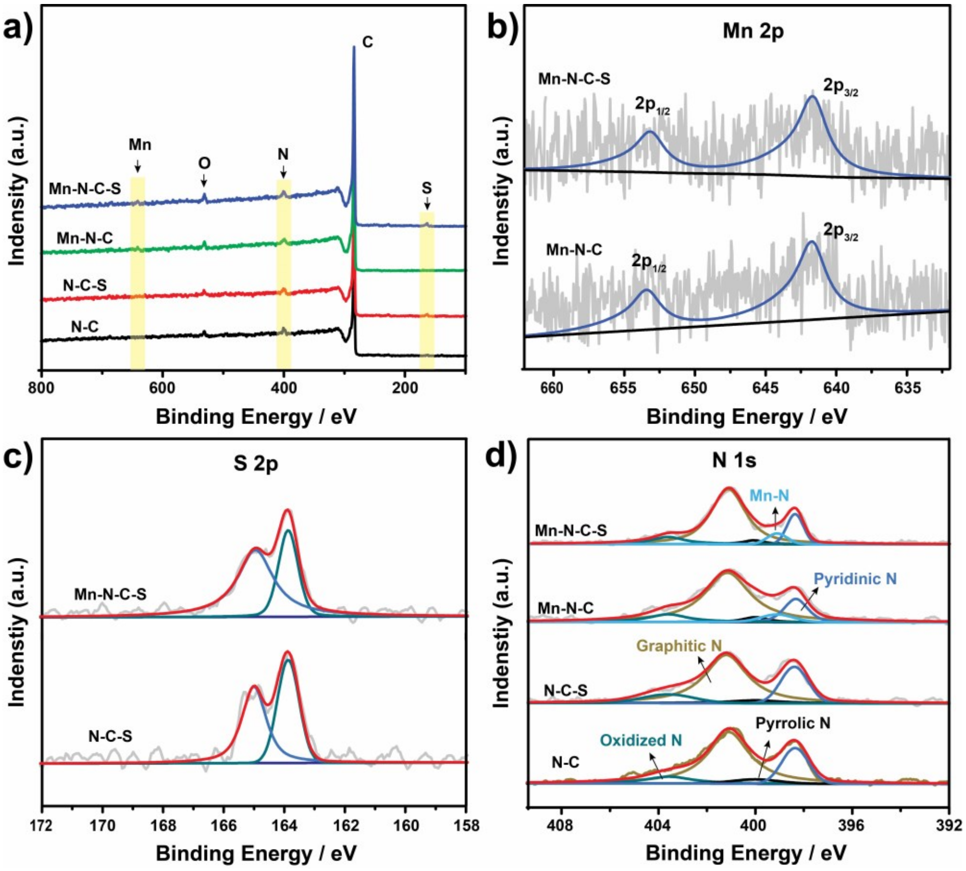

Figure 2. Compositional analysis of the samples. (a) XPS patterns of N-C, N-C-S, Mn-N-C, and Mn-N-C-S catalysts; (b) high-resolution Mn 2p XPS spectra of Mn-N-C and Mn-N-C-S catalysts; (c) high-resolution S 2p XPS spectra of N-C-S and Mn-N-C-S catalysts, and (d) high-resolution N 1s XPS spectra of N-C, N-C-S, Mn-N-C, and Mn-N-C-S catalysts.

X-ray photoelectron spectroscopy (XPS) was performed to determine the composition and chemical status in surface layers of catalysts. **Figure 2a** shows the wide-range spectra of N-C, N-C-S, Mn-N-C, and Mn-N-C-S catalysts. The spectra confirm the existence of N, S, and Mn elements in the Mn-N-C-S catalyst. The corresponding elemental composition of all four catalysts is summarized in **Table S2**. The S (0.8 at. %) content is about 2.7 times that of Mn (0.3 at. %). The ratio of sulfur/metal is higher than that of other S-doped catalysts (**Table S3**). All catalysts exhibited similar content and chemical state of the carbon in catalysts, suggesting no significant carbon structure difference (**Figure S6 and Table S4**). The atomic contents (0.3 at. %) of Mn in the Mn-N-C-S catalyst are the same as the Mn-N-C catalyst, suggesting that Mn-N-C and Mn-N-C-S catalysts have nearly a similar density of MnN_4 site. Such atomic content of Mn in the surface layer is comparable for the reported Fe and Co-doped catalysts with high ORR activity.[22, 40] Moreover, according to inductively coupled plasma mass spectrometry (ICP-MS), both Mn-N-C and Mn-N-C-S catalysts contain 0.039 and 0.038 wt. % Mn content, respectively, which are similar to other Mn-N-C catalysts.[43]

High-resolution XPS was used to further investigate the chemical changes of elements. As shown in **Figure 2b**, the oxidation state of Mn in both Mn-N-C and Mn-N-C-S catalysts were determined to be Mn^{2+} according to the binding energy of Mn $2p_{3/2}$ and Mn $2p_{1/2}$ centered at ca. 641.6 and 653.0 eV, respectively.[43] The same chemical state of Mn element for both catalysts suggests the S element has no substantial effect on the Mn-N-C-S catalyst's chemical valance due to the similar electronegativity (2.58) with C element (2.55).[44-45] The high-resolution S 2p spectra of the Mn-N-C-S catalyst were shown in **Figure 2c**, presenting two prominent peaks centered at ca. 163.9 and 165.0 eV, attributed to S $2p_{3/2}$ and S $2p_{1/2}$ peaks of thiophene-like structures (C-S-C) in the catalyst, respectively, indicative of doped S atoms in the carbon.[44, 46-47] The S doping in the Mn-N-C-S catalyst could be beneficial for improving ORR activity, as previously reported for S doped materials.[48-49] Moreover, the C-S-C structure is hydrophobic, which is favorable for improving water management and mass transfer in cathodes.[39] Also, the -SO_x group's signals in the Mn-N-C-S catalyst are not observed in the region from 167 to 172 eV.[45] No peak corresponded to the Mn-S bond can be found in the S 2p spectra. Thus, sulfur likely has no coordination with Mn in the carbon matrix, and no Mn-S compounds formed during the S doping process.[50] Only N is the ligand to coordinate with Mn sites in the catalyst.[51-52] So, it's essential to determine the forms of nitrogen for understanding Mn's coordination. Although the Mn doping leads to a slight decrease in the N content compared to the Mn-free samples, the amount of N appears to be adequate to form MnN_4 sites relative to Mn's low content (**Table S5**). The peaks at ca. 398.4, 399.9, 401.1, and 403.6 eV in the deconvoluted N 1s spectra (**Figure 2d**) stem from pyridinic-N, pyrrolic-N, graphitic-N, and oxidized-N, respectively.[53-54] For both Mn-N-C and Mn-N-C-S catalysts, the peak centered at 399.2 eV was observed in the spectra compared to others, likely corresponding to Mn-N coordination.[55]

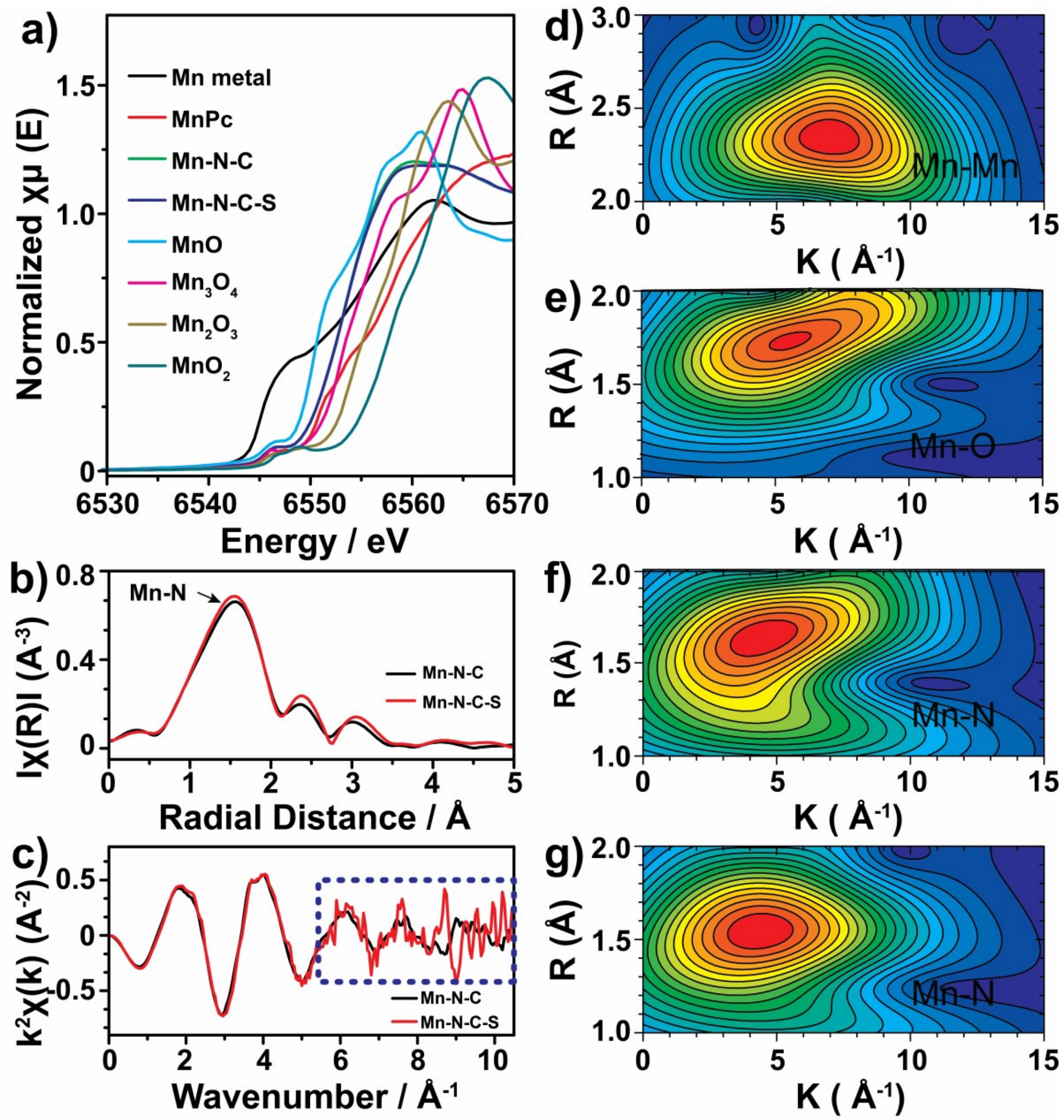

Figure 3. Structural characterization by XANES and EXAFS. (a) The experimental K-edge XANES spectra of Mn-N-C-S catalyst, Mn-N-C catalyst, and reference samples (Mn metal, MnO, MnO_2, Mn_2O_3, Mn_3O_4, and standard MnPc); (b) Fourier transforms of Mn K-edge EXAFS data of Mn-N-C and Mn-N-C-S catalyst; (c) EXAFS K-space of Mn-N-C and Mn-N-C-S catalyst; Wavelet Transform of Mn K-edge EXAFS (d) Mn metal, (e) MnO, (f) Mn-N-C, and (g) Mn-N-C-S catalyst.

The Mn-N coordination was investigated by X-ray absorption spectroscopy (XAS), including X-ray absorption near edge structure (XANES) and extended X-ray absorption fine structure (EXAFS) measurements at Mn K-edge. Several Mn-based materials (metallic Mn, MnO, Mn_3O_4, Mn_2O_3, MnO_2, and Mn phthalocyanine (MnPc)) were tested as the references to identify the state of Mn in the as-prepared samples. The Mn K-edge of the XANES spectrum (**Figure 3a**) clearly shows the adsorption edge of Mn-N-C-S between MnO and Mn_3O_4 but closer to MnO, suggesting the oxidation state of Mn species in the Mn-N-C-S is close to 2+, consistent with the above XPS analysis. The K edge of Mn-N-C catalyst resembles that of the Mn-N-C-S catalyst, indicating the oxidation state of Mn species in Mn-N-C is also approximately 2+. As shown in **Figure 3b**, the Fourier transform (FT) of the k^2-weighted EXAFS curves (FT-EXAFS) of the two catalysts show the prominent peak at around 1.55 Å, which is attributed to the scattering of Mn-N bonding. Meanwhile, no Mn-Mn contribution at around 2.3 Å can be found in the two catalysts. These results indicate that Mn-N-C and Mn-N-C-S catalysts have similar Mn-N coordination. The FT-EXAFS of the two catalysts does not entirely overlap, which implies that the S doping could affect the coordination environment of Mn atoms in the Mn-N-C-S catalyst. Impressively, the S doping effect is more clearly observed from 5.5 $Å^{-1}$ in K space of Mn, as depicted in **Figure 3c**. To more intuitively indicate the coordination of Mn, the Wavelet Transform (WT) EXAFS (WT-EXAFS) was also performed due to the powerful resolutions in K and R spaces. WT contour plots of Mn-N-C-S and Mn-N-C catalysts (**Figure 3f** and **g**) show the intensity peaks with the k value of 4.3 $Å^{-1}$ for the Mn-N bonding, which is clearly distinguished from the Mn metal (5.5 $Å^{-1}$) and MnO (7.0 $Å^{-1}$) (**Figure 3d** and **e**). This further confirms that Mn sites are atomically dispersed in Mn-N-C and Mn-N-C-S catalysts, consistent with the FT-EXAFS and the EELS results. Moreover, the Mn-N (1.55 Å) scattering path of the Mn-N-C-S catalyst observed in the R space is lower than that of the

Mn-N-C catalyst, thus verifying the effect of S doping on the coordination of Mn and implying the localization of S around the Mn-N coordination. Furthermore, the model-based EXAFS was carried out to further confirm the local structure of Mn-N-C and Mn-N-C-S catalysts, showing four N-coordinated structures (**Figure S7** and **Table S6**). According to the above analysis, it can be concluded that the Mn atom in the Mn-N-C-S catalyst is atomically embedded in the carbon matrix and coordinated with four N ligands.

The porous nature of the catalyst plays a vital role in boosting overall catalytic performance. The N_2 adsorption-desorption measurements were carried out to analyze the specific surface area and porosity of the studied catalysts. The S-doped samples exhibit larger adsorbed volumes than those of the sulfur-free samples (**Figure S8**). As listed in **Table S7**, the Mn-N-C-S catalyst has specific surface areas of 1114.83 m^2 g^{-1}, larger than that of the Mn-N-C catalyst (1009.48 m^2 g^{-1}). The high surface area of the Mn-N-C-S catalyst is ascribed to the introduction of defects by doping S. These results suggest the introduction of S element increases the specific surface area of the catalyst, consistent with the previously reported results.[56-57] Such a high specific surface facilitates the dispersion of active sites on the catalyst surface and mass transfer in fuel cells. Moreover, the sharp N_2 isotherm at a low-pressure range indicates the existence of a microporous structure. This is confirmed by pore size distribution curves of the Mn-N-C-S and Mn-N-C catalysts (**Figure S8b**). Most pore diameter falls in a range from 1 to 3 nm for both Mn-N-C-S and Mn-N-C catalysts. The pore size of catalysts affects the surface area and impacts the microstructure. The Zn evaporation during heat treatment creates interconnected pores inside and a lot of defects at the surface. The small pores prevent Mn and S sources from absorbing into the N-doped carbon interior, which could confine MnN_4 sites at the surface of N-doped carbon. The interconnected pores throughout the catalyst facilitate O_2 transport and provide accessibility to active sites. Raman spectra for all the catalysts were acquired (**Figure S9**). The ratio of D and G peak areas ($Area_D/Area_G$) can be used to profoundly investigate the effect of Mn and S doping on the graphitization of catalysts. As presented in **Table S8**, the high ratios indicate the highly disordered structure with abundant defects in the N-C, N-C-S, Mn-N-C, and Mn-N-C-S catalysts. Meanwhile, the S-containing samples show a higher ratio than those of the S-free samples, suggesting that the S doping introduced additional carbon structure defects.

Catalytic Activity and Stability. Polarization curves were recorded using a rotating ring disk electrode (RRDE) in O_2-saturated 0.5 M H_2SO_4 to investigate ORR activity of the studied catalysts (**Figure 4a**). The N-C catalyst shows inferior activity, which is similar to the previously reported metal-free catalysts.[58] In comparison, the half-wave potential ($E_{1/2}$) of the N-C-S catalyst is higher than that of the N-C catalyst, suggesting that the S doping is beneficial for enhancing catalytic activity. The same trend is also observed between Mn-N-C-S and Mn-N-C catalysts. The Mn-N-C-S catalyst displays a more positive $E_{1/2}$ (0.81 V) than the Mn-N-C catalyst ($E_{1/2} = 0.776$ V) under defined testing conditions. Moreover, the kinetic mass activity (j_m), which is usually used to assess the electrocatalytic activity of the PGM-free catalysts, was calculated using the Koutecky−Levich equation and then was normalized by the catalyst loading. The Mn-N-C-S catalyst exhibited a j_m of 1.85 mA mg^{-1} at 0.85 V, 2.06 times higher than that of the Mn-N-C catalyst (0.90 mA mg^{-1}). These results demonstrated the critical role of S atoms in enhancing the intrinsic activity of the MnN_4 site for the ORR. The H_2O_2 yield of the Mn-N-C-S catalyst is less than 1.0%, indicating a highly favorable selectivity for the four-electron reduction pathway (**Figure S10**). The yield of H_2O_2 increases to 2% on the Mn-N-C catalyst. As mentioned above, S doping can boost the ORR activity of catalysts through interaction with metal active center sites. Considering the similar nanostructure and density of the active sites on both Mn-N-C-S and Mn-N-C catalyst, as evidenced by EXAFS and XPS, the doped S likely promotes the intrinsic activity of the Mn-N-C-S catalyst.

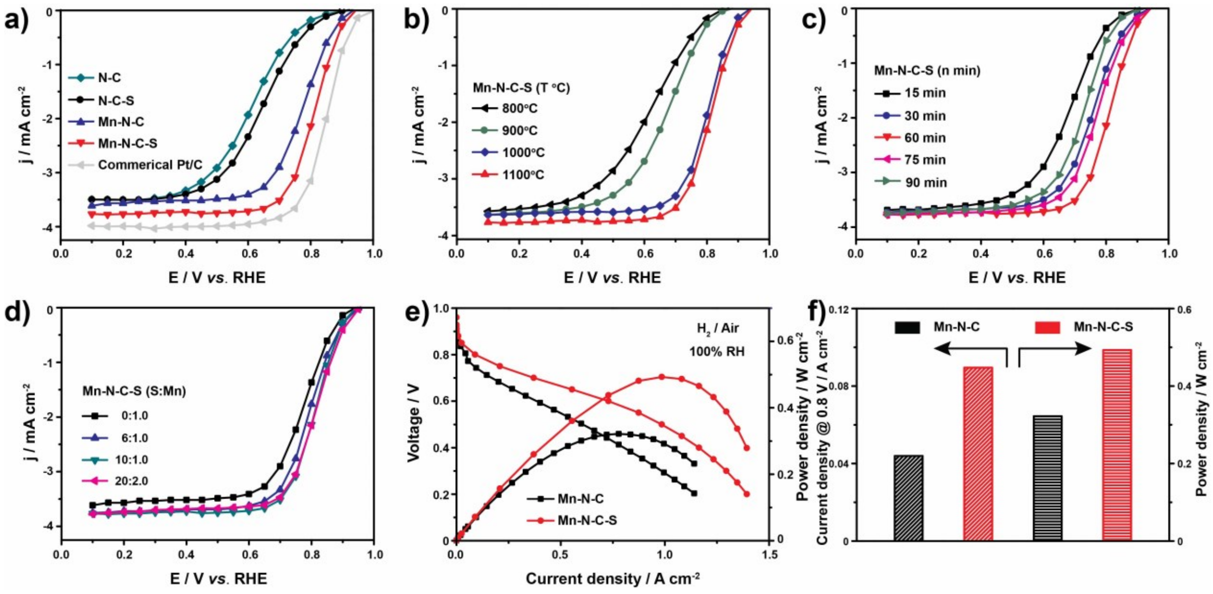

Figure 4. Electrochemical performance of different catalysts. (a) Steady-state ORR polarization plots for the N-C, N-C-S, Mn-N-C and Mn-N-C-S catalysts in 0.5 M H_2SO_4 and Pt/C catalyst (25 $\mu g_{Pt}/cm^2$) in 0.1 M $HClO_4$ at 25 ºC; ORR polarization of Mn-N-C-S catalysts synthesized (b) at various temperatures and (c) different heating times; (d) ORR polarization curves of the catalysts with different amount of S; (e) H_2-air fuel cell polarization plot of Mn-N-C and Mn-N-C-S catalysts, flow rate H_2/Air: 0.5/2.0 L min^{-1}, cell temperature: 80 °C, 2.0 bar back pressure; (f) comparisons of current density at 0.8 V and maximum power density for Mn-N-C and Mn-N-C-S catalysts in MEA.

Meanwhile, the $E_{1/2}$ of the Mn-N-C-S catalyst is only 50 mV lower than that of commercial Pt/C catalyst (25 μg_{Pt} cm^{-2}, $E_{1/2} = 0.86$ V in 0.1 M $HClO_4$ solution). To identify the leading active site of the catalyst, SCN^- and S^{2-} have been chosen as the chemical probes for the poisoning test due to the strong adsorption of both SCN^- and S^{2-} on metal sites of the catalyst.[59-60] **Figure S11** compares the ORR polarization curves of the Mn-N-C-S catalyst in the O_2-saturated 0.5 M H_2SO_4 solution before introducing 10 mM of poisoning ions. After adding the SCN^-, the onset potential declined to 0.80 V, and the $E_{1/2}$ significantly reduced to 0.71 V, but still higher than that of the N-C-S catalyst, which suggests the SCN^- ion blocked partial MnN_4 active sites. The reduced activity of the Mn-N-C-S catalyst was also observed after introducing S^{2-} in the O_2-saturated acidic solution. These results confirm that the Mn-doped catalysts' main active sites are MnN_4 sites embedded in the carbon matrix rather than metal-free CN_x.

To understand the influence of synthetic conditions on Mn-N-C-S catalyst activity, we carried out a series of control experiments, including the temperature, heating time, and precursor composition. The catalytic activity as a function of the heating temperature is shown in **Figure 4b**. The Mn-N-C-S (800 °C) catalyst obtained at 800 °C shows higher activity than the N-C catalyst but lower than the N-C-S catalyst. It suggests that S elements could be doped into the carbon support at 800 °C, which is not enough to form MnN_4 active sites in the carbon matrix. As the temperature was increased to 900 °C, the Mn-N-C-S (900 °C) catalyst shows higher activity than the N-C-S catalyst, implying that 900 °C should be the minimum temperature for the formation of MnN_4 active sites. According to the previous reports, high temperature is essential for forming a covalent C-S bond, which is the key to enhancing ORR activity.[45] When the temperature is further increased to 1000 °C, the Mn-N-C-S (1000 °C) catalyst presents significantly enhanced activity relative to the Mn-N-C catalyst but slightly lower than the Mn-N-C-S (1100 °C) catalyst prepared at 1100 °C. This result confirms the successful doping of S and the formation of abundant MnN_4 active sites at the elevated temperature. The zinc evaporation becomes more completed at higher heating temperatures. However, there is still a trace of zinc remaining in the catalyst after 1100 °C treatment, as evidenced by XPS and EDS. Based on the N-C and N-C-S catalysts' poor activity like “metal-free” carbon catalysts,[61] the residual Zn should have an insignificant effect on improving ORR activity. Fellinger *et al*. also reported that Zn-N_x sites play a negligible role in the ORR in acid media.[62]

As shown in **Figure 4c**, the influence of heating duration on the activity was also investigated at the optimal temperature of 1100 °C. The catalyst treated for 15 min exhibits an $E_{1/2}$ of 0.66 V, more positive than the N-C-S and Mn-N-C-S catalysts obtained at 900 °C, which suggests that the formation of MnN_4 active sites start at the initial stage of the treatment and the high temperature is a prerequisite for the formation of MnN_4 structure. With the heating duration increasing from 15 to 60 min, the catalyst activity increases, likely due to the increase in the number of MnN_4 active sites. However, when further increasing heating duration to 75 min, the $E_{1/2}$ negatively shifted to 0.77 V. As heating duration was increased up to 90 min, the ORR activity further decreases. The previous works reported that long-term high-temperature treatments significantly resulted in the evaporation and reduction of metal from the carbon matrix.[63-64] Thus, the declined activity during the prolonged heating treatment is mainly associated with the loss of Mn or N sites. Besides, the increased degree of graphitization likely reduces the defects and micropores to host MnN_4 active sites.

A series of catalysts with different S contents were prepared by varying the S/Mn ratio in the precursor for investigating the effect of S doping on the ORR activity of the MnN_4 site. **Figure 4d** displays the change of catalytic activity with various S/Mn ratios. When the S/Mn ratio is increased to 6 to 1, the catalyst presents increased activity compared to the S-free Mn-N-C catalyst. The catalytic activity is continuously improved with an increasing S/Mn ratio up to 10 to 1, further confirming that the S doping plays a vital role in enhancing ORR activity in acidic media. However, simultaneously doubling sulfur and manganese content (*i.e.*, the ratio of S/Mn is 20/2) does not further improve catalytic activity, implying that excessive S source would not increase the number of MnN_4 sites. This reveals that the adsorption capacity of carbon support is the major limitation to host more active sites. Thus, exploring innovative carbon hosts with sufficient porosity and defects is expected to further increase the dispersion of MnN_4 active sites.

We further incorporated the ORR catalyst into MEAs to evaluate the Mn-N-C-S catalyst performance in fuel cells. The MEA with a high catalyst loading of 7.5 mg cm^{-2} was tested initially at 2.0 bar backpressure of H_2/O_2 to determine the catalytic activity accurately without any mass transport limitation (**Figure S12**). The MEA displays an open-circuit voltage of 0.95 V, and the current density at 0.9 $V_{IR\text{-}free}$ reaches 20.6 mA cm^{-2}. These results further confirm the high intrinsic activity of the Mn-N-C-S catalyst in solid-state electrolyte environments within fuel cell electrodes. Furthermore, we compared the performance of Mn-N-C-S and Mn-N-C in an H_2-air cell (**Figure 4e**) at a backpressure of 2.0 bar and a typical loading of 4.0 mg cm^{-2}. The MEA using the Mn-N-C-S catalyst yields 370 mA cm^{-2} at 0.7 V, which significantly outperforms the Mn-N-C catalyst. Moreover, the Mn-N-C-S catalysts show better performance than the Mn-N-C catalyst at a low voltage range, indicating improved mass transfer. Considering the similar pore diameter distribution, the improved mass transfer originates from the S-induced large surface area and the C-S-C structure's hydrophobicity. Meanwhile, the fuel cell under H_2/air condition using Mn-N-C-S catalyst achieves a higher power density of 500 mW cm^{-2} as compared to 320 W cm^{-2} for the Mn-N-C catalyst (**Figure 4f**). This performance enhancement was also demonstrated at 1.0 bar backpressure (**Figure S13**), further confirming the enhanced kinetic activity and mass transport due to the S doping adjacent to MnN_4 active sites.

Mechanistic Understanding of Activity Improvement. The first-principles density functional theory (DFT) calculations were performed to gain insights into S doping's role in promoting catalytic activity of Mn-N-C catalyst. In our previous study,[2] we predicted that two types of MnN_4 structures. One was embedded intact in a graphene layer (denoted as MnN_4C_{10} and shown in **Figure 5a**), and the other was embedded near a microspore in a graphene layer (denoted as MnN_4C_{12} and shown in **Figure S15a**). Here, we investigated how the S dopant could affect the ORR activity of two types of MnN_4 sites. In consistent with this experimental result, we assumed that a single S dopant is bonded on the graphene layer containing an MnN_4C_{10} or MnN_4C_{12} active site. To identify the binding site of S on a graphene layer containing an MnN_4C_{10} site, we have compared the system energies of multiple adsorption configurations, as depicted in **Figure S14** and **Table S9**. The DFT predicts that the single-atom S dopant is energetically most favorable to be adsorbed on a bridging site between two carbon atoms adjacent to the MnN_4C_{10} site. Hence, we employed this site (denoted as MnN_4C_{10}-S and shown in **Figure 5b**) to model the S-doped MnN_4C_{10} site in our catalysts. Similarly, we constructed an MnN_4C_{12}-S (as shown in **Figure S15b**) site to model the S-doped MnN_4C_{12} site.

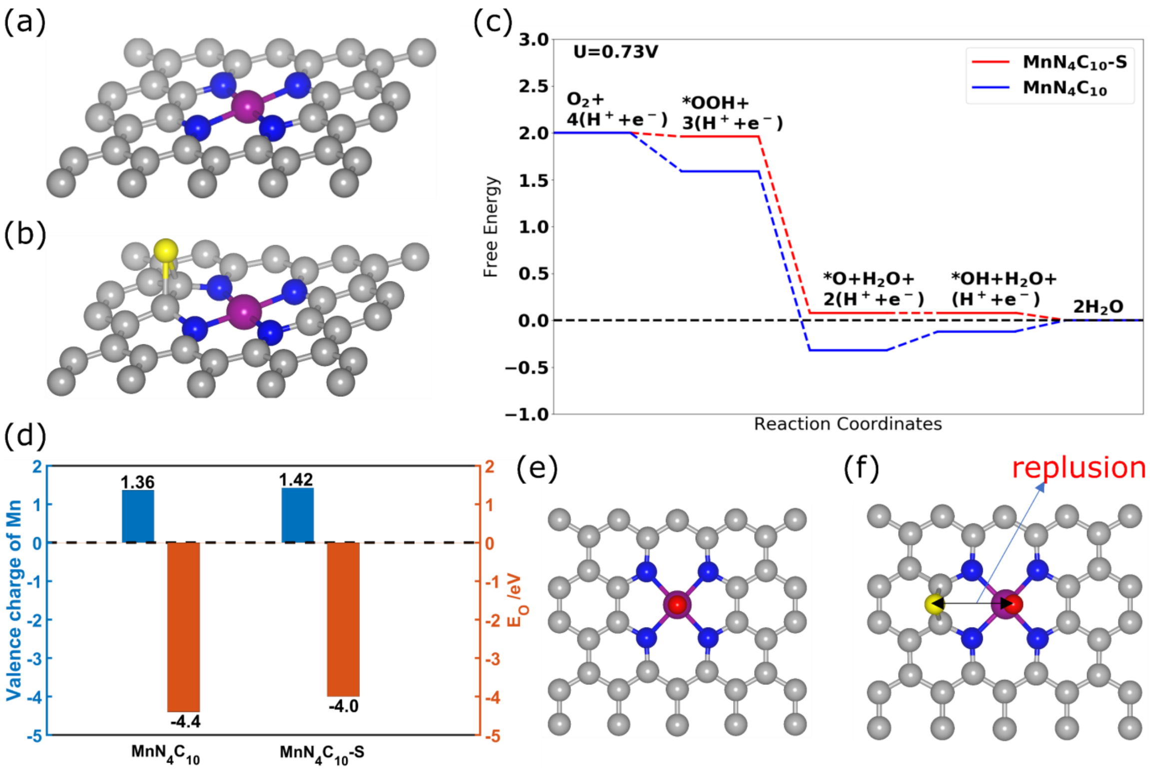

Figure 5. Atomic structure of (a) MnN_4C_{10} and (b) MnN_4C_{10}-S sites. (c) Calculated free energy evolution diagram of ORR following an associative pathway on MnN_4C_{10} and MnN_4C_{10}-S sites under an electrode potential of U=0.73V. (d) The calculated valence charge (blue) and adsorption energy of O (orange) on the central Mn atom in MnN_4C_{10} and MnN_4C_{10}-S sites. Optimized atomic adsorption configurations of O on (e) MnN_4C_{10} and (f) MnN_4C_{10}-S sites. The gray, blue, purple, red, and yellow balls represent C, N, Mn, O, and S atoms, respectively.

We calculated the free energy evolution diagrams of the ORR on the thus-constructed MnN_4C_{10}-S and MnN_4C_{12}-S sites using the computational hydrogen electrode method.[65] We adopted a 4e^- associative pathway for the ORR, in which an O_2 molecule would adsorb on the top of the central Mn atom, then be protonated to form OOH, OH, and H_2O sequentially. **Figure 5c** shows that the free energy change for all the elementary steps on the MnN_4C_{10}-S site becomes negative under an applied electrode potential of 0.73V, which is defined as the limiting potential for the ORR on this site. In contrast, the limiting potential of the MnN_4C_{10} site without S doping is predicted to be only 0.54 V. This result suggests that S dopant could thermodynamically improve the limiting potential of the ORR on the MnN_4C_{10}-S site compared to the MnN_4C_{10} site. However, the difference in the limiting potential on the MnN_4C_{12}-S and MnN_4C_{12} sites was insignificant (0.79 *vs*. 0.80 V), suggesting that S dopant has little effect on the MnN_4C_{12}-S site as compared to the more active MnN_4C_{10} site from the thermodynamic point of view.

Previously reported studies on S-doped Fe-N-C catalysts have demonstrated that the increase in activity is mainly due to the regulation of the charge of the Fe center by the S dopant.[38] We carried out the Bader charge analysis[66-67] to find the valence charge of the central Mn site in MnN_4C_{10} with and without a S dopant. As presented in **Figure 5d**, we predicted that the valence charge of the central Mn was +1.36 on the MnN_4C_{10} site and +1.42 on the MnN_4C_{10}-S site. This result indicates that the S dopant only induces a small (about 4%) change in the charge state at the Mn site and implies that the small change is not the main factor for the increased activity, unlike the S-doped Fe-N-C catalysts.[37-38] More importantly, we compared in **Figure 5d** the calculated adsorption energies of O (denoted as E_O) on the MnN_4C_{10}-S and MnN_4C_{10} sites. A reduction of 9% in the adsorption energy of O on the MnN_4C_{10}-S is calculated than the MnN_4C_{10} site. Examining the O adsorption configurations in **Figure 5e** and **f**, we found a clear spatial repulsion interaction between the S dopant and ORR intermediates such as *O. Therefore, we believe that the spatial effect stemmed from the repulsive interaction between S dopant and the ORR intermediate species led to weakened adsorption of ORR intermediates and hence enhanced ORR activity at the MnN_4C_{10}-S site.

Catalyst Degradation Behavior. The MEA stability test was performed at 0.65 V for 15 h under H_2/air condition at 80 ^oC to investigate the Mn-N-C-S catalyst degradation behavior. The performance loss of the catalysts is displayed in **Figure 6a**. The degradation curves show two apparent regions: the initial fast decay and the slow decay regions. The Mn-N-C-S catalysts exhibited a degradation rate (6.0% per hour) in the first 5 hours, which is higher than the rate of the Mn-N-C catalyst (2.9%). In the slow decay region, the decay rates of Mn-N-C and Mn-N-C-S catalysts are 1.4% and 2.1%, respectively. After 10 hours, 60% current density of the Mn-N-C-S MEA was retained, lower than that (78.4%) of Mn-N-C MEA (**Figure 6b**). The relative fast decay indicates that the S-doping decreases the stability of the Mn-N-C-S catalyst. The Mn-N-C-S MEA before and after the 5-h test was characterized by busing STEM to investigate the catalyst decay mechanisms. The fresh MEA showed a uniform and porous catalyst layer structure (**Figure 6c$_1$** and **Figure S16a**). After 5 hours of testing, the cathode catalyst layer barely underwent structural changes (**Figure 6c$_3$** and **Figure S16c**), which implies the decay should not stem from the structural change of the MEA. The cyclic voltammetry curves before and after constant voltage tests were compared. After holding a constant voltage at 0.65 V for 19 h, the double-layer capacitance did not change significantly (**Figure 6d**), indicating no structural change of the carbon in MEAs. **Figure 6c$_2$ and c$_4$** further compare the atomic structure of the catalysts before and after the 5-hour test. Compared with the fresh cathode catalyst layer (**Figure 6c$_2$** and **Figure S16b**), the bright areas can be observed in the decayed catalyst (**Figure 6c$_4$** and **Figure S16d**), which can be attributed to the Mn agglomeration. These results indicate that the agglomeration of partial Mn is one reason for the degradation of the Mn-N-C-S catalyst. This structural change should be associated with the fact that the S doping reduces the graphitization degree of the Mn-N-C-S catalyst, as evidenced by Raman spectra, thus impacting the stability of the MnN_4 structure.

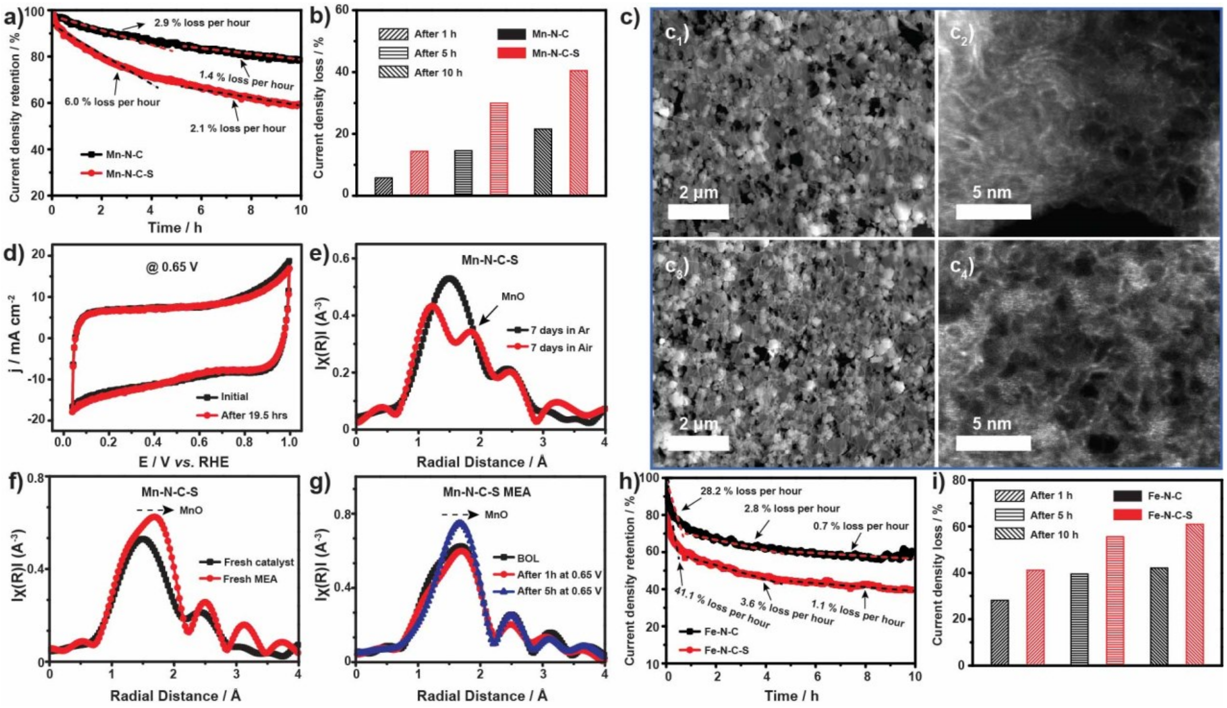

Figure 6. (a) Stability tests for Mn-N-C and Mn-N-C-S catalysts at a constant potential of 0.65 V under H_2/air conditions; (b) the comparison of current density loss of Mn-N-C and Mn-N-C-S catalysts after 1, 5, and 10 h test at 0.65 V; (c) STEM images of Mn-N-C-S MEA before (c_1 and c_2) and after (c_3 and c_4) 5 h test; (d) fuel cell CV curves of Mn-N-C-S MEA before and after potential cycling stability tests (0.60-0.95 V, 10,000 cycles) under H_2/air; Fourier transforms of Mn K-edge EXAFS data of (e) Mn-N-C-S catalysts stored in Ar and air for 7 days, (f) Mn-N-C-S catalysts and fresh M-N-C-S MEA, and (g) M-N-C-S MEA before and after 1 and 5 h test at a constant potential of 0.65 V; (h) stability tests for Fe-N-C and Fe-N-C-S catalysts at a constant potential of 0.65 V under H_2/air conditions, and (i) the comparison of current density loss of Fe-N-C and Fe-N-C-S catalysts after 1, 5, and 10 h test at 0.65 V.

The FT-EXAFS has been employed to further explore the structure change process of the MnN_4 sites under various environments. As shown in **Figure 6e**, the prominent peak in the FT-EXAFS of catalysts stored in Ar for 7 days locates at around 1.52 Å, which is almost the same as the fresh catalyst. However, after storing in the air for 7 days, the main peak splits into two peaks assigned to Mn-O distance in MnO_x. These results suggest that the Mn-N-C-S catalyst has a strong affinity for oxygen, and the degradation of MnN_4 site has started since the catalysts were exposed to air. After assembling the catalyst into the MEA, the prominent peak becomes broader with a shoulder peak and shifts to around 1.78 Å that corresponds to the distance between Mn and O in MnO (**Figure 6f**). Therefore, MEA fabrication includes ink preparation, and the hot-pressing process can partially change the MnN_4 structures in the catalyst. With increasing testing hours, the shoulder peak disappears, and the central peak is located at 1.78 Å after the 5-h test (**Figure 6g**), suggesting that more MnN_4 sites combine with the O elements. These FT-EXAFS results demonstrate that the MnN_4 site oxidation is still a challenge in maintaining stability for the Mn-N-C-S catalyst. Based on the above results, we can conclude that the oxidation and agglomeration of the MnN_4 site occur simultaneously in the catalytic process and are the primary mechanisms for the performance decay of the Mn-N-C-S catalyst in fuel cells.

Compared to the most popular Fe-N-C catalysts' stability, both Fe-N-C and Fe-N-C-S catalysts (synthesis details in supporting information) were tested at a constant voltage of 0.65 V for 10 hours. **Figure 6h** shows the degradation curves of Fe-N-C and Fe-N-C-S catalysts. Unlike the slow decay of Mn-N-C and Mn-N-C-S catalysts, both Fe-N-C and Fe-N-C-S catalysts exhibit dramatic decay in the first hour: 28.2% and 41.1% of activity loss for the Fe-N-C and the Fe-N-C-S, respectively (**Figure 6h**). These results indicate the fragile stability of the FeN_4 structure. Despite the slow degradation rate in the next 9 hours, there are only 57.9% and 39.1% activity retaining for the Fe-N-C and Fe-N-C-S catalysts, respectively (**Figure 6i**). These comparisons indicate that the Mn-N-C-S catalyst still has relatively better stability than the Fe-N-C and Fe-N-C-S catalysts and demonstrates that the S doping is an effective way to improve the catalytic activity of the

MnN_4 site without significantly hampering the stability of the catalyst. Similar to other M-N-C catalysts,[68] the Mn-N-C-S catalyst shows insufficient stability. However, the promotional S doping is verified to enhance the MnN_4 site's intrinsic activity by increasing limiting potential and weakening ORR intermediate adsorption. Further regulating the coordination environment of MnN_4 sites could mitigate the possible agglomeration/oxidation of the MnN_4 sites during the ORR.[69] Besides, strengthening local carbon structure with enhanced oxidation resistance to stabilize MnN_4 sites in catalysts is critical for achieving a trade-off between the activity and stability.[70]

CONCLUSIONS

In summary, we explored an S-doped atomically dispersed single metal MnN_4 site catalyst (Mn-N-C-S) in the absence of any metal clusters and aggregates through an effective adsorption-pyrolysis process. Unlike prior works that enhanced the catalyst activity by increasing the density of active sites, we improved the intrinsic activity of the MnN_4 sites by introducing S dopants while maintaining a high density of the active site. The critical factors including related structure and catalytic properties were comprehensively investigated for the Mn-N-C-S catalyst. During the synthesis, the sulfur source does not interfere Mn adsorption and the subsequent MnN_4 formation. On the contrary, S doping dramatically boosts the intrinsic activity of MnN_4 sites for the ORR in acidic media. The obtained Mn-N-C-S catalyst exhibited enhanced catalytic performance, including more positive half-wave potential, increased kinetic current density, and improved MEA performance in fuel cells. The enhanced intrinsic activity of the MnN_4 sites originates from the increased limiting potentials and favorable kinetics during the ORR. In particular, theoretic calculations revealed that the S dopant leads to a repulsive interaction with the ORR intermediate species adsorbed on the MnN_4 sites, thus weakening their adsorption and facilitating the desorption process. Moreover, the S doping increases the Mn-N-C-S catalyst's surface area and creates the hydrophobic C-S-C groups next to MnN_4 sites, facilitating oxygen transport and water removal. These benefits make Mn-N-C-S catalyst generated a compelling MEA performance, *i.e.*, 370 mA/cm^2 at 0.7 V and a peak power density of 500 mW cm^{-2}, representing one of the best PGM-free and Fe-free catalysts.

However, like other studied M-N-C catalysts, the Mn-N-C-S catalyst still suffers from significant activity loss, especially at the initial stage during the ORR. We employed advanced electron microscopy and FT-EXAFS analysis to elucidate the possible catalyst degradation mechanisms. Compared to other possible reasons, the Mn oxidation and agglomeration happened even during the storage and MEA fabrication happened, converting highly active MnN_4 site to MnO species, which are primarily responsible for the ORR activity loss of the Mn-N-C-S catalyst. Also, the S doping to carbon structures adjacent to the MnN_4 sites likely accelerates the degradation process. Therefore, continuous effort is needed to increase the degree of graphitization in local carbon structures[71] and modify the electron structure surrounding MnN_4 sites through optimal dopings, aiming to achieve an activity-stability trade-off.

METHODS

Catalyst Synthesis. Thiourea (127 mg, 1.6 mmol), and $MnCl_2$ (20 mg, 0.16 mmol) were first dissolved in 2 ml solution (1 ml isopropanol, 1 ml 0.25 M HCl), followed by sonicating for 5 min. The solution was added into a vial, including ZIF-8-derived N-doped nanocarbon (NC) powder (20 mg). Then, 0.2 ml of 2.0 M HCl solution was added to the vial to avoid hydrolysis of $MnCl_2$. The mixture was sonicated for 30 min blow 18 °C and stirred for at least two hours. Then collect the precipitants by centrifuge without washing. The precipitants were dried under a vacuum oven at 50 °C for 12 h. The dried precipitants were treated at 1100 °C for one hour under Agron. The heating rate was 37 ºC min^{-1}. The final product was denoted as Mn-N-C-S catalyst. For the comparison, the Mn-N-C, N-C-S, and N-C catalysts were prepared by the same procedure without adding thiourea, $MnCl_2$, and the mixture of $MnCl_2$ and thiourea, respectively.

Material Characterization. The morphology of catalysts was investigated by scanning electron microscopy (SEM) on a Hitachi SU 70 microscope. The crystal phases of all catalysts were identified *via* powder X-ray diffraction (XRD) on a Rigaku Ultima IV diffractometer with Cu K-α X-rays. X-ray photoelectron spectroscopy (XPS) was performed on a Kratos AXIS Ultra DLD XPS system equipped with a hemispherical energy analyzer and a monochromatic Al Kα source. The monochromatic Al Kα source was operated at 15 keV and 150 W; pass energy was fixed at 40 eV for the high-resolution scans. The N_2 isothermal adsorption/desorption was recorded at 77 K on a Micromeritics TriStar II. Samples were degassed at 150 °C for 5 h under vacuum before nitrogen physisorption measurements. The inductively coupled plasma mass spectrometry (ICP-MS) was performed to determine the metal contents in catalysts. Transmission electron microscopy (TEM), including high-resolution TEM (HRTEM), high angle annular dark-field scanning TEM (HAADF-STEM), and electron energy loss spectroscopy (EELS) mapping, were performed at BNL on a probe-corrected FEI Titan 80-300 S/TEM equipped with a gatan EELS detector. Raman spectroscopy was conducted by using a Renishaw Raman system at 514 nm excitation. Mn K-edge X-ray absorption near edge structure (XANES) and extended X-ray absorption fine structure (EXAFS) experiments were carried out at beamline 12BM, Advanced Photon Source (APS), Argonne National Laboratory (ANL). Data reduction, data analysis, and EXAFS analysis were performed with the Athena, Artemis, and IFEFFIT software packages. For model-based EXAFS analysis, all the scattering paths were generated by the FEFF calculation function in Artemis based on the crystal structure of MnPc. The amplitude reduction factor (S_0^2) values were then calculated by performing the FEFFIT on the EXAFS data of the reference sample (MnPc). With S_0^2 known, the EXAFS data of the catalyst was fitted with such generated amplitudes to calculate the coordination number. Wavelet Transform was performed with the HAMA Fortran Version of Wavelet Transform.

Electrochemical Measurements. All electrochemical measurements were performed by using a CHI Electrochemical Station (Model 760b) in a three-electrode cell at room temperature. A glassy carbon rotating ring disk electrode (RRDE), Hg/$HgSO_4$ (K_2SO_4-sat.) electrode, and graphite rod were chosen as the working, reference, and counter electrodes, respectively. Each catalyst was uniformly dispersed in the mixing solution of isopropanol and Nafion (5 wt %). The ink was cast onto the RRDE with a designed loading of 0.8 mg cm^{-2} and dried at room temperature. The catalyst was activated by cyclic voltammetry in N_2-saturated 0.5 M H_2SO_4 electrolyte at a scan rate of 50 mV s^{-1}. Then, the ORR activity of as-prepared catalysts was tested on the RRDE by steady-state measurement using staircase voltammetry with a step of 0.05 V at intervals of 30 s from 1.0 to 0.1 V *vs*. RHE in O_2-saturated 0.5 M H_2SO_4 solution at 25 °C with a rotation rate of 900 rpm. The obtained current curves are normalized by the geometric area of the RRDE.

Fuel Cell Test. The Mn-N-C-S catalyst was loaded on the cathode side for MEA tests. The mixture of the catalyst, 1-proponal, de-ionized water, and Nafion suspension was stirred in an ice bath for 3 hours. The inks were brushed on the carbon paper until the catalyst loading reached ~7.5 mg cm^{-2} for the activity test and ~4.0 mg cm^{-2} for H_2-air performance evaluation. The GDE with Pt (0.25 mg_{Pt} cm^{-2}) was used as the anode. The MEA of the cathode, Nafion 212 membrane, and the anode was assembled by hot-pressing at 135 °C, 5 MPa for 5 min. The single cell with an active geometric area of 5.0 cm^2 was then evaluated in a test station (100 W, Scribner 850e, Scribner Associates). Air (or oxygen) and H_2 (purity 99.99%) flowing were used as the cathode and anode reactants for MEA tests.

Computational Method. The spin-polarized density functional theory (DFT) calculations with a plane-wave basis set were carried out using the Vienna *ab Initio* simulation package (VASP) code. Projector augmented wave (PAW) pseudopotential was employed to describe the core electrons. Electronic exchange and correlation terms were described by generalized gradient approximation (GGA) of the Perdew, Burke, and Ernzernhof (PBE) functionals. In all calculations, the cutoff energy of 400 eV was set to expand the wave functions. The Brillouin Zone was sampled using the Monkhorst 4×4×1 k-point grid for MnN_4C_{10} and MnN_4C_{10}-S, 3×3×1 k-point grid for MnN_4C_{12} and MnN_4C_{12}-S. Bader charge analysis was used to obtain the distribution of electrons. In Bader charge analysis, the Brillouin Zone was sampled using the Monkhorst 8×8×1 k-point grid for MnN_4C_{10} and MnN_4C_{10}-S. A vacuum region of 14 Å thick was added in the direction normal to the graphene layer to ensure negligible interaction between periodic images. Optimized structures were obtained until the force fell below 0.02eV/ Å.

In our calculations, the computational hydrogen electrode (CHE) method was used to calculate the free energy of all elementary steps of ORR. Incorporating the electrochemical potential in CHE, the free energy of a single proton-electron pair is defined as -eU relative to one-half of the free energy of H_2 molecule in the gas phase at standard condition, in which U is the electrode potential concerning the reversible hydrogen electrode (RHE). Detailed calculation methods are supplied in the Supporting Information.

ASSOCIATED CONTENT

Supporting Information

The Supporting Information is available free of charge at https://pubs.acs.org/doi/10.1021/acsnano.xxxxx.

More detailed experimental details for catalyst synthesis and materials characterization; additional material characterization, including SEM, TEM, XPS, BET, and XRD results and discussion to elucidate materials properties; additional electrochemical measurements and fuel cell testing results to demonstrate promising catalyst performance; detailed computational methods to provide an insightful understanding of S doping to boost catalyst activity for the ORR.

AUTHOR INFORMATION

Corresponding Authors

Gang Wu−*Department of Chemical and Biological Engineering, University at Buffalo, The State University of New York, Buffalo, NY 14260, USA*; orcid.org/0000-0003-0885-6172; E-mail: gangwu@buffalo.edu

Zhenxing Feng−*School of Chemical Biological, and Environmental Engineering, Oregon State University, Corvallis, OR 97331, USA*; orcid.org/0000-0001-7598-5076; E-mail: zhenxing.feng@oregonstate.edu

Guofeng Wang−*Department of Mechanical Engineering and Materials Science, University of Pittsburgh, Pittsburgh, PA 15260, USA*; orcid.org/0000-0001-8249-4101; E-mail: guw8@pitt.edu

Hui Xu−*Giner Inc, Newton, MA 02466, USA*; E-mail: hxu@ginerinc.com

Authors

Lin Guo−*Department of Chemical and Biological Engineering, University at Buffalo, The State University of New York, Buffalo, NY 14260, USA*

Sooyeon Hwang–*Center for Functional Nanomaterials Brookhaven National Laboratory Upton, NY 11973, USA*

Boyang Li–*Department of Mechanical Engineering and Materials Science, University of Pittsburgh, Pittsburgh, PA 15260, USA*

Fan Yang–*Giner Inc, Newton, MA 02466, USA*

Maoyu Wang–*School of Chemical Biological, and Environmental Engineering, Oregon State University, Corvallis, OR 97331, USA*

Mengjie Chen–*Department of Chemical and Biological Engineering, University at Buffalo, The State University of New York, Buffalo, NY 14260, USA*

Xiaoxuan Yang–*Department of Chemical and Biological Engineering, University at Buffalo, The State University of New York, Buffalo, NY 14260, USA*

Stavros G. Karakalos–*Department of Chemical Engineering, University of South Carolina, Columbia, SC 29208, USA*

David A. Cullen–*Materials Science and Technology Division, Oak Ridge National Laboratory, Oak Ridge, TN 37831, USA*

Author Contributions

≠L. G., S. H., and B. L. contributed equally to this work.

Author Contributions

L. G. and G. Wu conceived and designed this work; L. G., S. H., M. W., and M. C. performed the experiments and characterizations; B. L. accomplished calculations and simulations; L. G. and F. Y. carried out the testing and analyzed the data; L. G. wrote the manuscript; X. Y. revised the manuscript; Z. F., G. Wang, G. Wu, and H. X supervised the project. All authors have approved the final version of the manuscript.

Notes

The authors declare no competing financial interest.

ACKNOWLEDGMENTS

We are grateful for the financial support from U. S. Department of Energy, Fuel Cell Technologies Office (DE-EE0008075), and the ElectroCat Consortium. This research used beamline 7-BM (QAS) of the National Synchrotron Light Source II, a U.S. Department of Energy (DOE) Office of Science User Facility operated for the DOE Office of Science by Brookhaven National Laboratory. The DFT calculations used the computational resources provided by the University of Pittsburgh Center for Research Computing and the Extreme Science and Engineering Discovery Environment (XSEDE) supported by the National Science Foundation grant number ACI-1053575.

REFERENCES

(1) Li, J.; Jiao, L.; Wegener, E.; Richard, L. L.; Liu, E.; Zitolo, A.; Sougrati, M. T.; Mukerjee, S.; Zhao, Z.; Huang, Y.; Yang, F.; Zhong, S.; Xu, H.; Kropf, A. J.; Jaouen, F.; Myers, D. J.; Jia, Q., Evolution Pathway from Iron Compounds to Fe_1(II)–N_4 Sites through Gas-Phase Iron during Pyrolysis. *J. Am. Chem. Soc.* **2020**, *142* (3), 1417-1423.

(2) Li, J.; Chen, M.; Cullen, D. A.; Hwang, S.; Wang, M.; Li, B.; Liu, K.; Karakalos, S.; Lucero, M.; Zhang, H.; Lei, C.; Xu, H.; Sterbinsky, G. E.; Feng, Z.; Su, D.; More, K. L.; Wang, G.; Wang, Z.; Wu, G., Atomically Dispersed Manganese Catalysts for Oxygen Reduction in Proton-Exchange Membrane Fuel Cells. *Nat. Catal.* **2018**, *1* (12), 935-945.

(3) Xie, X.; He, C.; Li, B.; He, Y.; Cullen, D. A.; Wegener, E. C.; Kropf, A. J.; Martinez, U.; Cheng, Y.; Engelhard, M. H.; Bowden, M. E.; Song, M.; Lemmon, T.; Li, X. S.; Nie, Z.; Liu, J.; Myers, D. J.; Zelenay, P.; Wang, G.; Wu, G.; et al., Performance Enhancement and Degradation Mechanism Identification of a Single-Atom Co–N–C Catalyst for Proton Exchange Membrane Fuel Cells. *Nat. Catal.* **2020**, *3* (12), 1044-1054.

(4) Wang, X. X.; Swihart, M. T.; Wu, G., Achievements, Challenges and Perspectives on Cathode Catalysts in Proton Exchange Membrane Fuel Cells for Transportation. *Nat. Catal.* **2019**, *2* (7), 578-589.

(5) Wang, Y.; Su, H.; He, Y.; Li, L.; Zhu, S.; Shen, H.; Xie, P.; Fu, X.; Zhou, G.; Feng, C.; Zhao, D.; Xiao, F.; Zhu, X.; Zeng, Y.; Shao, M.; Chen, S.; Wu, G.; Zeng, J.; Wang, C., Advanced Electrocatalysts with Single-Metal-Atom Active Sites. *Chem. Rev.* **2020**, *120* (21), 12217-12314.

(6) Martinez, U.; Komini Babu, S.; Holby, E. F.; Chung, H. T.; Yin, X.; Zelenay, P., Progress in the Development of Fe-Based PGM-Free Electrocatalysts for the Oxygen Reduction Reaction. *Adv. Mater.* **2019**, *31* (31), 1806545.

(7) Du, L.; Prabhakaran, V.; Xie, X.; Park, S.; Wang, Y.; Shao, Y., Low-PGM and PGM-Free Catalysts for Proton Exchange Membrane Fuel Cells: Stability Challenges and Material Solutions. *Adv. Mater.* **2021**, *33*, 1908232.

(8) Shao, Y.; Dodelet, J.-P.; Wu, G.; Zelenay, P., PGM-Free Cathode Catalysts for PEM Fuel Cells: A Mini-Review on Stability Challenges. *Adv. Mater.* **2019**, *31* (31), 1807615.

(9) Zhang, H.; Chung, H. T.; Cullen, D. A.; Wagner, S.; Kramm, U. I.; More, K. L.; Zelenay, P.; Wu, G., High-Performance Fuel Cell Cathodes Exclusively Containing Atomically Dispersed Iron Active Sites. *Energy Environ. Sci.* **2019**, *12* (8), 2548-2558.

(10) Chen, M.; He, Y.; Spendelow, J. S.; Wu, G., Atomically Dispersed Metal Catalysts for Oxygen Reduction. *ACS Energy Lett.* **2019**, *4* (7), 1619-1633.

(11) Spier, E.; Neuenschwander, U.; Hermans, I., Insights into the Cobalt(II)-Catalyzed Decomposition of Peroxide. *Angew. Chem. Int. Ed.* **2013**, *52* (5), 1581-1585.

(12) Li, Y.; Wang, H.; Priest, C.; Li, S.; Xu, P.; Wu, G., Advanced Electrocatalysis for Energy and Environmental Sustainability *via* Water and Nitrogen Reactions. *Adv. Mater.* **2021**, *33* (6), 2000381.

(13) Wang, X. X.; Prabhakaran, V.; He, Y.; Shao, Y.; Wu, G., Iron-Free Cathode Catalysts for Proton-Exchange-Membrane Fuel Cells: Cobalt Catalysts and the Peroxide Mitigation Approach. *Adv. Mater.* **2019**, *31* (31), 1805126.

(14) Zhong, Y.; Liang, X.; He, Z.; Tan, W.; Zhu, J.; Yuan, P.; Zhu, R.; He, H., The Constraints of Transition Metal Substitutions (Ti, Cr, Mn, Co and Ni) in Magnetite on Its Catalytic Activity in Heterogeneous Fenton and UV/Fenton Reaction: From the Perspective of Hydroxyl Radical Generation. *Appl. Catal. B: Environ.* **2014**, *150-151*, 612-618.

(15) Zhu, G.; Liu, F.; Wang, Y.; Wei, Z.; Wang, W., Systematic Exploration of N, C Coordination Effects on the ORR Performance of Mn–N_x Doped Graphene Catalysts Based on DFT Calculations. *Phys. Chem. Chem. Phys.* **2019**, *21* (24), 12826-12836.

(16) Liu, K.; Qiao, Z.; Hwang, S.; Liu, Z.; Zhang, H.; Su, D.; Xu, H.; Wu, G.; Wang, G., Mn- and N- Doped Carbon as Promising Catalysts for Oxygen Reduction Reaction: Theoretical Prediction and Experimental Validation. *Appl. Catal. B: Environ.* **2019**, *243*, 195-203.

(17) Zhang, W.; Mao, K.; Zeng, X. C., B-Doped MnN_4-G Nanosheets as Bifunctional Electrocatalysts for Both Oxygen Reduction and Oxygen Evolution Reactions. *ACS Sustain. Chem. Eng.* **2019**, *7* (22), 18711-18717.

(18) Peng, H.; Liu, F.; Liu, X.; Liao, S.; You, C.; Tian, X.; Nan, H.; Luo, F.; Song, H.; Fu, Z.; Huang, P., Effect of Transition Metals on the Structure and Performance of the Doped Carbon Catalysts Derived from Polyaniline and Melamine for ORR Application. *ACS Catal.* **2014**, *4* (10), 3797-3805.

(19) Sahraie, N. R.; Kramm, U. I.; Steinberg, J.; Zhang, Y.; Thomas, A.; Reier, T.; Paraknowitsch, J.-P.; Strasser, P., Quantifying the Density and Utilization of Active Sites in Non-Precious Metal Oxygen Electroreduction Catalysts. *Nat. Commun.* **2015**, *6* (1), 8618.

(20) Sun, Y.; Silvioli, L.; Sahraie, N. R.; Ju, W.; Li, J.; Zitolo, A.; Li, S.; Bagger, A.; Arnarson, L.; Wang, X.; Moeller, T.; Bernsmeier, D.; Rossmeisl, J.; Jaouen, F.; Strasser, P., Activity–Selectivity Trends in the Electrochemical Production of Hydrogen Peroxide over Single-Site Metal–Nitrogen–Carbon Catalysts. *J. Am. Chem. Soc.* **2019**, *141* (31), 12372-12381.

(21) He, Y.; Hwang, S.; Cullen, D. A.; Uddin, M. A.; Langhorst, L.; Li, B.; Karakalos, S.; Kropf, A. J.; Wegener, E. C.; Sokolowski, J.; Chen, M.; Myers, D.; Su, D.; More, K. L.; Wang, G.; Litster, S.; Wu, G., Highly Active Atomically Dispersed CoN_4 Fuel Cell Cathode Catalysts Derived from Surfactant-Assisted MOFs: Carbon-Shell Confinement Strategy. *Energy Environ. Sci.* **2019**, *12* (1), 250-260.

(22) Wang, X. X.; Cullen, D. A.; Pan, Y.-T.; Hwang, S.; Wang, M.; Feng, Z.; Wang, J.; Engelhard, M. H.; Zhang, H.; He, Y.; Shao, Y.; Su, D.; More, K. L.; Spendelow, J. S.; Wu, G., Nitrogen-Coordinated Single Cobalt Atom Catalysts for Oxygen Reduction in Proton Exchange Membrane Fuel Cells. *Adv. Mater.* **2018**, *30* (11), 1706758.

(23) He, Y.; Shi, Q.; Shan, W.; Li, X.; Kropf, A. J.; Wegener, E. C.; Wright, J.; Karakalos, S.; Su, D.; Cullen, D. A.; Wang, G.; Myers, D. J.; Wu, G., Dynamically Unveiling Metal–Nitrogen

Coordination during Thermal Activation to Design High-Efficient Atomically Dispersed CoN_4 Active Sites. *Angew. Chem. Int. Ed.* **2021**, doi: 10.1002/anie.202017288.

(24) He, Y.; Guo, H.; Hwang, S.; Yang, X.; He, Z.; Braaten, J.; Karakalos, S.; Shan, W.; Wang, M.; Zhou, H.; Feng, Z.; More, K. L.; Wang, G.; Su, D.; Cullen, D. A.; Fei, L.; Litster, S.; Wu, G., Single Cobalt Sites Dispersed in Hierarchically Porous Nanofiber Networks for Durable and High-Power PGM-Free Cathodes in Fuel Cells. *Adv. Mater.* **2020**, *32* (46), 2003577.

(25) Shi, Q.; Hwang, S.; Yang, H.; Ismail, F.; Su, D.; Higgins, D.; Wu, G., Supported and Coordinated Single Metal Site Electrocatalysts. *Mater. Today* **2020**, *37*, 93-111.

(26) Bai, L.; Duan, Z.; Wen, X.; Si, R.; Guan, J., Atomically Dispersed Manganese-Based Catalysts for Efficient Catalysis of Oxygen Reduction Reaction. *Appl. Catal. B: Environ.* **2019**, *257*, 117930.

(27) Shi, Q.; He, Y.; Bai, X.; Wang, M.; Cullen, D. A.; Lucero, M.; Zhao, X.; More, K. L.; Zhou, H.; Feng, Z.; Liu, Y.; Wu, G., Methanol Tolerance of Atomically Dispersed Single Metal Site Catalysts: Mechanistic Understanding and High-Performance Direct Methanol Fuel Cells. *Energy Environ. Sci.* **2020**, *13* (10), 3544-3555.

(28) Mukherjee, S.; Yang, X.; Shan, W.; Samarakoon, W.; Karakalos, S.; Cullen, D. A.; More, K.; Wang, M.; Feng, Z.; Wang, G.; Wu, G., Atomically Dispersed Single Ni Site Catalysts for Nitrogen Reduction toward Electrochemical Ammonia Synthesis Using N_2 and H_2O. *Small Methods* **2020**, *4* (6), 1900821.

(29) Liu, S.; Wang, M.; Yang, X.; Shi, Q.; Qiao, Z.; Lucero, M.; Ma, Q.; More, K. L.; Cullen, D. A.; Feng, Z.; Wu, G., Chemical Vapor Deposition for Atomically Dispersed and Nitrogen Coordinated Single Metal Site Catalysts. *Angew. Chem. Int. Ed.* **2020**, *59* (48), 21698-21705.

(30) Zhao, X.; Yang, X.; Wang, M.; Hwang, S.; Karakalos, S.; Chen, M.; Qiao, Z.; Wang, L.; Liu, B.; Ma, Q.; Cullen, D. A.; Su, D.; Yang, H.; Zang, H.-Y.; Feng, Z.; Wu, G., Single-Iron Site Catalysts with Self-Assembled Dual-Size Architecture and Hierarchical Porosity for Proton-Exchange Membrane Fuel Cells. *Appl. Catal. B: Environ.* **2020**, *279*, 119400.

(31) Mohd Adli, N.; Shan, W.; Hwang, S.; Samarakoon, W.; Karakalos, S.; Li, Y.; Cullen, D. A.; Su, D.; Feng, Z.; Wang, G.; Wu, G., Engineering Atomically Dispersed FeN_4 Active Sites for CO_2 Electroreduction. *Angew. Chem. Int. Ed.* **2021**, *60* (2), 1022-1032.

(32) Chen, M.; Li, X.; Yang, F.; Li, B.; Stracensky, T.; Karakalos, S.; Mukerjee, S.; Jia, Q.; Su, D.; Wang, G.; Wu, G.; Xu, H., Atomically Dispersed MnN_4 Catalysts *via* Environmentally Benign Aqueous Synthesis for Oxygen Reduction: Mechanistic Understanding of Activity and Stability Improvements. *ACS Catal.* **2020**, *10* (18), 10523-10534.

(33) Jiang, W.-J.; Gu, L.; Li, L.; Zhang, Y.; Zhang, X.; Zhang, L.-J.; Wang, J.-Q.; Hu, J.-S.; Wei, Z.; Wan, L.-J., Understanding the High Activity of Fe–N–C Electrocatalysts in Oxygen Reduction: Fe/Fe_3C Nanoparticles Boost the Activity of Fe–N_x. *J. Am. Chem. Soc.* **2016**, *138* (10), 3570-3578.

(34) Zheng, Y.; Jiao, Y.; Ge, L.; Jaroniec, M.; Qiao, S. Z., Two-Step Boron and Nitrogen Doping in Graphene for Enhanced Synergistic Catalysis. *Angew. Chem. Int. Ed.* **2013**, *52* (11), 3110-3116.

(35) Dong, Y.; Zhou, M.; Tu, W.; Zhu, E.; Chen, Y.; Zhao, Y.; Liao, S.; Huang, Y.; Chen, Q.; Li, Y., Hollow Loofah-Like N, O-Co-Doped Carbon Tube for Electrocatalysis of Oxygen Reduction. *Adv. Funct. Mater.* **2019**, *29* (18), 1900015.

(36) Wang, Y.-C.; Lai, Y.-J.; Song, L.; Zhou, Z.-Y.; Liu, J.-G.; Wang, Q.; Yang, X.-D.; Chen, C.; Shi, W.; Zheng, Y.-P.; Rauf, M.; Sun, S.-G., S-Doping of an Fe/N/C ORR Catalyst for Polymer Electrolyte Membrane Fuel Cells with High Power Density. *Angew. Chem. Int. Ed.* **2015**, *54* (34), 9907-9910.

(37) Shen, H.; Gracia-Espino, E.; Ma, J.; Zang, K.; Luo, J.; Wang, L.; Gao, S.; Mamat, X.; Hu, G.; Wagberg, T.; Guo, S., Synergistic Effects between Atomically Dispersed Fe−N−C and C−S−C for the Oxygen Reduction Reaction in Acidic Media. *Angew. Chem. Int. Ed.* **2017**, *56* (44), 13800-13804.

(38) Zhang, J.; Zhao, Y.; Chen, C.; Huang, Y.-C.; Dong, C.-L.; Chen, C.-J.; Liu, R.-S.; Wang, C.; Yan, K.; Li, Y.; Wang, G., Tuning the Coordination Environment in Single-Atom Catalysts to Achieve Highly Efficient Oxygen Reduction Reactions. *J. Am. Chem. Soc.* **2019**, *141* (51), 20118-20126.

(39) Seredych, M.; László, K.; Bandosz, T. J., Sulfur-Doped Carbon Aerogel as a Metal-Free Oxygen Reduction Catalyst. *ChemCatChem* **2015**, *7* (18), 2924-2931.

(40) Zhang, H.; Hwang, S.; Wang, M.; Feng, Z.; Karakalos, S.; Luo, L.; Qiao, Z.; Xie, X.; Wang, C.; Su, D.; Shao, Y.; Wu, G., Single Atomic Iron Catalysts for Oxygen Reduction in Acidic Media: Particle Size Control and Thermal Activation. *J. Am. Chem. Soc.* **2017**, *139* (40), 14143-14149.

(41) Huang, P.; Li, H.; Huang, X.; Chen, D., Multiheteroatom-Doped Porous Carbon Catalyst for Oxygen Reduction Reaction Prepared Using 3D Network of ZIF-8/Polymeric Nanofiber as a Facile-Doping Template. *ACS Appl. Mater. Interfaces.* **2017**, *9* (25), 21083-21088.

(42) Ni, B.; Chen, R.; Wu, L.; Xu, X.; Shi, C.; Sun, P.; Chen, T., Optimized Enhancement Effect of Sulfur in Fe–N–S Codoped Carbon Nanosheets for Efficient Oxygen Reduction Reaction. *ACS Appl. Mater. Interfaces.* **2020**, *12* (21), 23995-24006.

(43) Guan, J.; Duan, Z.; Zhang, F.; Kelly, S. D.; Si, R.; Dupuis, M.; Huang, Q.; Chen, J. Q.; Tang, C.; Li, C., Water Oxidation on a Mononuclear Manganese Heterogeneous Catalyst. *Nat. Catal.* **2018**, *1* (11), 870-877.

(44) Liang, J.; Jiao, Y.; Jaroniec, M.; Qiao, S. Z., Sulfur and Nitrogen Dual-Doped Mesoporous Graphene Electrocatalyst for Oxygen Reduction with Synergistically Enhanced Performance. *Angew. Chem. Int. Ed.* **2012**, *51* (46), 11496-11500.

(45) Yang, Z.; Yao, Z.; Li, G.; Fang, G.; Nie, H.; Liu, Z.; Zhou, X.; Chen, X. a.; Huang, S., Sulfur-Doped Graphene as an Efficient Metal-Free Cathode Catalyst for Oxygen Reduction. *ACS Nano* **2012**, *6* (1), 205-211.

(46) Yang, S.; Zhi, L.; Tang, K.; Feng, X.; Maier, J.; Müllen, K., Efficient Synthesis of Heteroatom (N or S)-Doped Graphene Based on Ultrathin Graphene Oxide-Porous Silica Sheets for Oxygen Reduction Reactions. *Adv. Funct. Mater.* **2012**, *22* (17), 3634-3640.

(47) Jin, H.; Zhou, H.; Li, W.; Wang, Z.; Yang, J.; Xiong, Y.; He, D.; Chen, L.; Mu, S., *In Situ* Derived Fe/N/S-Codoped Carbon Nanotubes from ZIF-8 Crystals as Efficient Electrocatalysts for the Oxygen Reduction Reaction and Zinc–Air Batteries. *J. Mater. Chem. A* **2018**, *6* (41), 20093-20099.

(48) Wang, Y. C.; Lai, Y. J.; Song, L.; Zhou, Z. Y.; Liu, J. G.; Wang, Q.; Yang, X. D.; Chen, C.; Shi, W.; Zheng, Y. P.; Rauf, M.; Sun, S. G., S-Doping of an Fe/N/C ORR Catalyst for Polymer Electrolyte Membrane Fuel Cells with High Power Density. *Angew. Chem. Int. Ed.* **2015**, *54* (34), 9907-10.

(49) Li, Q.; Chen, W.; Xiao, H.; Gong, Y.; Li, Z.; Zheng, L.; Zheng, X.; Yan, W.; Cheong, W. C.; Shen, R.; Fu, N.; Gu, L.; Zhuang, Z.; Chen, C.; Wang, D.; Peng, Q.; Li, J.; Li, Y., Fe Isolated

Single Atoms on S, N Codoped Carbon by Copolymer Pyrolysis Strategy for Highly Efficient Oxygen Reduction Reaction. *Adv. Mater.* **2018**, *30* (25), e1800588.

(50) Gao, X.; Wang, B.; Zhang, Y.; Liu, H.; Liu, H.; Wu, H.; Dou, S., Graphene-Scroll-Sheathed α-MnS Coaxial Nanocables Embedded in N, S Co-Doped Graphene Foam as 3D Hierarchically Ordered Electrodes for Enhanced Lithium Storage. *Energy Stor. Mater.* **2019**, *16*, 46-55.

(51) Lefevre, M.; Proietti, E.; Jaouen, F.; Dodelet, J. P., Iron-Based Catalysts with Improved Oxygen Reduction Activity in Polymer Electrolyte Fuel Cells. *Science* **2009**, *324* (5923), 71-4.

(52) Liu, Q.; Li, Q.; Chen, S., Metal–Nitrogen Coordination Moieties in Carbon for Effective Electrocatalytic Reduction of Oxygen. *Curr. Opin. Electrochem.* **2020**, *21*, 46-54.

(53) Shen, H.; Gracia-Espino, E.; Ma, J.; Zang, K.; Luo, J.; Wang, L.; Gao, S.; Mamat, X.; Hu, G.; Wagberg, T.; Guo, S., Synergistic Effects between Atomically Dispersed Fe-N-C and C-S-C for the Oxygen Reduction Reaction in Acidic Media. *Angew. Chem. Int. Ed.* **2017**, *56* (44), 13800-13804.

(54) Xiao, Y.-P.; Jiang, W.-J.; Wan, S.; Zhang, X.; Hu, J.-S.; Wei, Z.-D.; Wan, L.-J., Self-Deposition of Pt Nanocrystals on Mn_3O_4 Coated Carbon Nanotubes for Enhanced Oxygen Reduction Electrocatalysis. *J. Mater. Chem. A* **2013**, *1* (25), 7463-7468.

(55) Zhang, B.; Zhang, J.; Shi, J.; Tan, D.; Liu, L.; Zhang, F.; Lu, C.; Su, Z.; Tan, X.; Cheng, X.; Han, B.; Zheng, L.; Zhang, J., Manganese Acting as a High-Performance Heterogeneous Electrocatalyst in Carbon Dioxide Reduction. *Nat. Commun.* **2019**, *10* (1), 2980.

(56) Qiao, Y.; Yuan, P.; Hu, Y.; Zhang, J.; Mu, S.; Zhou, J.; Li, H.; Xia, H.; He, J.; Xu, Q., Sulfuration of an Fe-N-C Catalyst Containing Fe_xC/Fe Species to Enhance the Catalysis of Oxygen Reduction in Acidic Media and for Use in Flexible Zn-Air Batteries. *Adv. Mater.* **2018**, *30* (46), e1804504.

(57) Liu, S.; Cai, Y.; Zhao, X.; Liang, Y.; Zheng, M.; Hu, H.; Dong, H.; Jiang, S.; Liu, Y.; Xiao, Y., Sulfur-Doped Nanoporous Carbon Spheres with Ultrahigh Specific Surface Area and High Electrochemical Activity for Supercapacitor. *J. Power Sources* **2017**, *360*, 373-382.

(58) Shui, J.; Wang, M.; Du, F.; Dai, L., N-Doped Carbon Nanomaterials Are Durable Catalysts for Oxygen Reduction Reaction in Acidic Fuel Cells. *Sci. Adv.* **2015**, *1* (1), e1400129.

(59) Wang, Q.; Zhou, Z.-Y.; Lai, Y.-J.; You, Y.; Liu, J.-G.; Wu, X.-L.; Terefe, E.; Chen, C.; Song, L.; Rauf, M.; Tian, N.; Sun, S.-G., Phenylenediamine-Based FeN_x/C Catalyst with High Activity for Oxygen Reduction in Acid Medium and Its Active-Site Probing. *J. Am. Chem. Soc.* **2014**, *136* (31), 10882-10885.

(60) Liang, H.-W.; Brüller, S.; Dong, R.; Zhang, J.; Feng, X.; Müllen, K., Molecular Metal–N_x Centres in Porous Carbon for Electrocatalytic Hydrogen Evolution. *Nat. Commun.* **2015**, *6* (1), 7992.

(61) Wu, G.; More, K. L.; Johnston, C. M.; Zelenay, P., High-Performance Electrocatalysts for Oxygen Reduction Derived from Polyaniline, Iron, and Cobalt. *Science* **2011**, *332* (6028), 443-447.

(62) Menga, D.; Ruiz-Zepeda, F.; Moriau, L.; Šala, M.; Wagner, F.; Koyutürk, B.; Bele, M.; Petek, U.; Hodnik, N.; Gaberšček, M.; Fellinger, T.-P., Active-Site Imprinting: Preparation of Fe–N–C Catalysts from Zinc Ion–Templated Ionothermal Nitrogen-Doped Carbons. *Adv. Energy Mater.* **2019**, *9* (43), 1902412.

(63) Wei, S.; Li, A.; Liu, J.-C.; Li, Z.; Chen, W.; Gong, Y.; Zhang, Q.; Cheong, W.-C.; Wang, Y.; Zheng, L.; Xiao, H.; Chen, C.; Wang, D.; Peng, Q.; Gu, L.; Han, X.; Li, J.; Li, Y., Direct Observation of Noble Metal Nanoparticles Transforming to Thermally Stable Single Atoms. *Nat. Nanotechnol.* **2018**, *13* (9), 856-861.

(64) Li, J.; Zhang, H.; Samarakoon, W.; Shan, W.; Cullen, D. A.; Karakalos, S.; Chen, M.; Gu, D.; More, K. L.; Wang, G.; Feng, Z.; Wang, Z.; Wu, G., Thermally Driven Structure and Performance Evolution of Atomically Dispersed FeN_4 Sites for Oxygen Reduction. *Angew. Chem. Int. Ed.* **2019**, *58* (52), 18971-18980.

(65) Norskov, J. K.; Rossmeisl, J.; Logadottir, A.; Lindqvist, L.; Kitchin, J. R.; Bligaard, T.; Jonsson, H., Origin of the Overpotential for Oxygen Reduction at a Fuel-Cell Cathode. *J. Phys. Chem. B* **2004**, *108* (46), 17886-17892.

(66) Sanville, E.; Kenny, S. D.; Smith, R.; Henkelman, G., Improved Grid-Based Algorithm for Bader Charge Allocation. *J. Comput. Chem.* **2007**, *28* (5), 899-908.

(67) Yu, M.; Trinkle, D. R., Accurate and Efficient Algorithm for Bader Charge Integration. *J. Chem. Phys.* **2011**, *134* (6), 064111.

(68) He, Y.; Liu, S.; Priest, C.; Shi, Q.; Wu, G., Atomically Dispersed Metal–Nitrogen–Carbon Catalysts for Fuel Cells: Advances in Catalyst Design, Electrode Performance, and Durability Improvement. *Chem. Soc. Rev.* **2020**, *49* (11), 3484-3524.

(69) Zhu, Y.; Sokolowski, J.; Song, X.; He, Y.; Mei, Y.; Wu, G., Engineering Local Coordination Environments of Atomically Dispersed and Heteroatom-Coordinated Single Metal Site Electrocatalysts for Clean Energy-Conversion. *Adv. Energy Mater.* **2020**, *10* (11), 1902844.

(70) Liu, S.; Shi, Q.; Wu, G., Solving the Activity–Stability Trade-Off Riddle. *Nat. Catal.* **2021**, *4* (1), 6-7.

(71) Qiao, Z.; Hwang, S.; Li, X.; Wang, C.; Samarakoon, W.; Karakalos, S.; Li, D.; Chen, M.; He, Y.; Wang, M.; Liu, Z.; Wang, G.; Zhou, H.; Feng, Z.; Su, D.; Spendelow, J. S.; Wu, G., 3D Porous Graphitic Nanocarbon for Enhancing the Performance and Durability of Pt Catalysts: A Balance between Graphitization and Hierarchical Porosity. *Energy Environ. Sci.* **2019**, *12* (9), 2830-2841.

Table of Contents